Engineering dynamical phase diagrams with driven lattices in spinor gases

J. O. Austin-Harris , ¹ Z. N. Hardesty-Shaw , ¹ Q. Guan , ^{2,3,4} C. Binegar , ¹ D. Blume , ^{2,3} R. J. Lewis-Swan, ^{2,3,*} and Y. Liu , ¹, [†]

¹Department of Physics, Oklahoma State University, Stillwater, Oklahoma 74078, USA

²Homer L. Dodge Department of Physics and Astronomy, University of Oklahoma, Norman, Oklahoma 73019, USA

³Center for Quantum Research and Technology, University of Oklahoma, Norman, Oklahoma 73019, USA

⁴Department of Physics and Astronomy, Washington State University, Pullman, Washington 99164, USA

(Received 14 August 2023; accepted 20 March 2024; published 10 April 2024)

We experimentally demonstrate that well-designed driven lattices are versatile tools to simultaneously tune multiple key parameters (spin-dependent interactions, spinor phase, and quadratic Zeeman energy) for manipulating phase diagrams of spinor gases with negligible heating and atom losses. This opens avenues for studying engineered Hamiltonians and dynamical phase transitions. Modulation-induced harmonics generate progressively narrower separatrices at driving-frequency-determined higher magnetic-field strengths. This technique enables exploration of multiple, previously inaccessible parameter regimes of spinor dynamics (notably high magnetic-field strengths, tunable spinor phase, and individually tunable spin-preserving and spin-changing collisions) and widens the range of cold-atom applications, e.g., in quantum sensing and studies of nonequilibrium dynamics.

DOI: 10.1103/PhysRevA.109.043309

I. INTRODUCTION

The high degree of controllability available in latticeconfined spinor Bose-Einstein condensates (BECs) provides an ideal platform for quantum simulation of a wide range of interesting phenomena, spanning from nonequilibrium dynamics and dynamical phase transitions to the production of massively entangled spin singlets with immediate applications in quantum enhanced sensing [1-23]. These and many other spinor phenomena are induced by interconversions of multiple spin components and therefore determined by the competition of the quadratic Zeeman energy q and the spin-dependent interaction c_2 [4–23]. Due to intrinsically small values of c_2 in many atomic species, studies of spinor physics and its applications have mainly been restricted to a regime with small values of q comparable to c_2 , e.g., weak magnetic fields, motivating an extensive search for methods of manipulating these quantities [7–20]. For example, c_2 can be tuned by changing the atomic density, confining atoms into static optical lattices, or altering scattering lengths near Feshbach resonances, while q can be manipulated by dressing fields induced by offresonant microwave pulses or linearly polarized off-resonant laser beams [18–29]. However, these techniques are limited by heating and atom losses for substantial changes; therefore, significant spinor physics remains restricted to relatively small net q [18–25]. Changing the relative phase θ among spin states can also drastically alter spinor dynamics, although it has been much less explored in the literature due to technical challenges in precisely detecting and tuning θ [8,11–15,18–23].

In this paper we present a versatile technique for manipulating dynamical phase diagrams of spinor gases by

sinusoidally driving the depth of a one-dimensional (1D) optical lattice at a frequency f much larger than the typical scale of c_2 . Our data demonstrate that well-designed driven lattices can simultaneously tune multiple key parameters (including spin-dependent interactions, θ , and q) that determine spinor physics with negligible heating and atom losses. Prior studies of spin dynamics in free space (no lattices) have identified a diverging oscillation period at a critical quadratic Zeeman energy q^* , associated with the crossing of a separatrix in the underlying classical phase space that marks a dynamical phase transition [30,31]. We observe that the driven lattices create additional dynamical critical points at q^* approximately symmetric about q/h = f/2 [where (\hbar) h is the (reduced) Planck constant], with progressively narrower critical regions occurring whenever q/h is an integer multiple of f/2 due to lattice-modulation-induced higher harmonics. We understand these observations with a dynamical single-spatial-mode approximation (DSMA) (see Appendixes A and B) [20]. This article demonstrates that multiple, previously inaccessible parameter regimes of spinor dynamics, e.g., high magnetic-field strengths, precisely tuned θ , and individually tunable spinpreserving and spin-changing collisions, can be conveniently explored using driven lattices. This technique enables expanded applications of spinor gases in, e.g., quantum sensing, Hamiltonian engineering, and the study of nonequilibrium dynamics, over a wide working range.

II. EXPERIMENTAL PROCEDURE AND RESULTS

In each experimental cycle, we prepare an F=1 BEC of up to 10^5 sodium atoms at an initial state of $\rho_0 \approx 0.5$, $\theta=0$, and magnetization $M=\rho_1-\rho_{-1}=0$ at t=0 in a crossed optical dipole trap (ODT) at a desired lattice depth $u_L(0)$ and q. Here ρ_{m_F} is the fractional population in the $|F=1,m_F\rangle$ state and $\theta=\theta_{m_F=1}+\theta_{m_F=-1}-2\theta_{m_F=0}$ is the

^{*}lewisswan@ou.edu

[†]yingmei.liu@okstate.edu

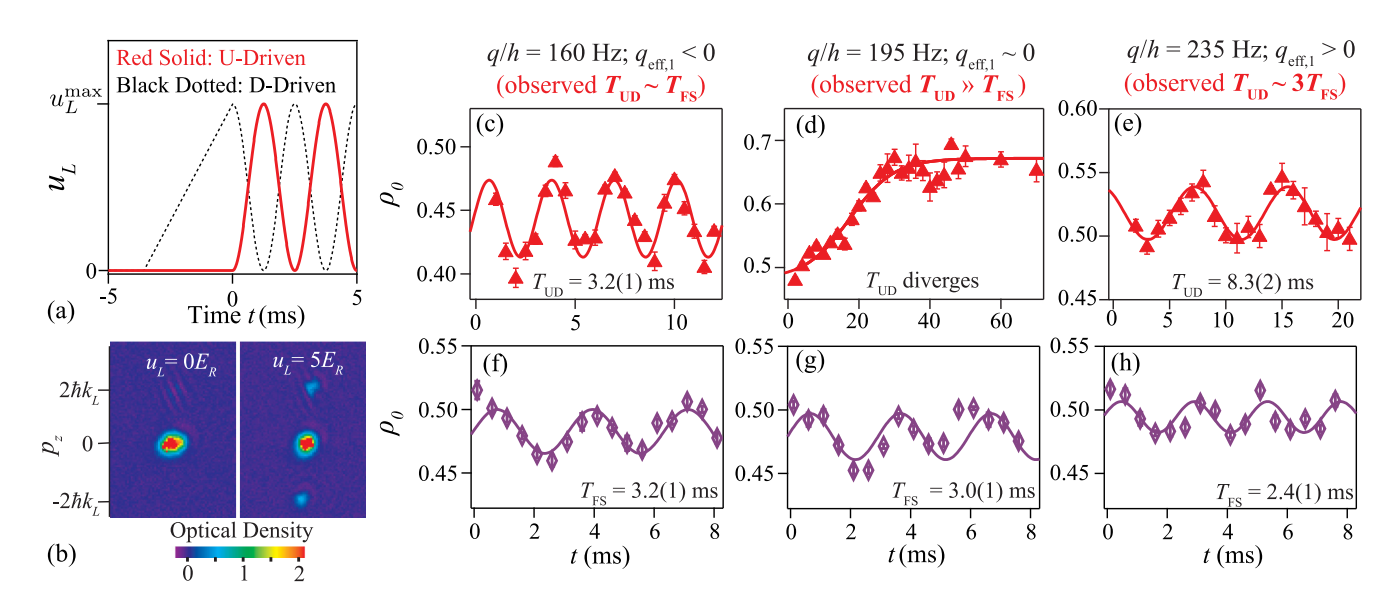


FIG. 1. (a) Solid and dotted lines display the timing of *U*-driven and *D*-driven lattice sequences, respectively. (b) TOF images taken via *U*-driven sequences at the minimum (left) and maximum (right) lattice depths, showing atoms occupying different momentum p states. Here k_L is the lattice wave vector. (c)–(e) Triangles display observed spin oscillations near $q^*/h \approx f/2 = 200$ Hz via *U*-driven sequences when q/h equals (c) 160 Hz, (d) 195 Hz, and (e) 235 Hz. (f)–(h) Similar to (c)–(e) but taken in free space. Solid lines in (c)–(h) are sinusoidal or sigmoidal fits (see Appendix D).

relative phase among the three spin states. While the atoms are held in the ODT of trapping frequencies $\omega_{x,y,z} \sim 2\pi \times (120, 120, 150)$ Hz, the depth of a shallow 1D optical lattice, with a lattice spacing of 532 nm, is sinusoidally driven at a frequency f between 0 and the maximum lattice depth u_L^{\max} , i.e., $u_L(t) = (u_L^{\max}/2)[1 + \cos(2\pi ft - \phi)]$ with $\phi = 0$ ($\phi = \pi$) for D-driven (U-driven) sequences [see Fig. 1(a)] for a variable time t. The lattice driving frequency investigated in this paper, f = 400 Hz, is separated from the ODT trapping frequencies and their multiples, which may explain the observed negligible heating and atom losses. We then abruptly release the atoms from all trapping potentials and detect the atoms via spin-resolved imaging after time of flight (TOF) ballistic expansion [10,18].

The driven lattice induces oscillations of the momentum distributions [Fig. 1(b)] and a periodic spin-dependent interaction given by $c_2(t) = \mathcal{G}_0 + \sum_{k=1}^{\infty} \mathcal{G}_k \cos(k2\pi ft - \phi_k)$. The index k arises because $c_2(t)$ is only approximately sinusoidal; the higher harmonics (k > 1) therefore have nonzero contributions to the dynamics (see Appendixes A and C). Here \mathcal{G}_0 (\mathcal{G}_k) is a positive interaction strength controlling the spinpreserving (spin-changing) collisions (see Appendix C). The phase ϕ_k is determined by the specific driven lattice sequence, for example, $\phi_1 = \phi$ and $\phi_2 = 2\phi + \pi$ for our experimental sequences (see Appendix C). In this work $c_2/h \sim 25$ Hz in free space. For all driven lattice sequences we set $u_L^{\text{max}} =$ $5E_R$, where E_R is the recoil energy, yielding $\mathcal{G}_1/\mathcal{G}_0 \sim 0.2$ with $\mathcal{G}_0/h \sim 30$ Hz and $\mathcal{G}_1/h \sim 5$ Hz (see Appendix B). For our system, where M=0 and $hf\gg \mathcal{G}_0$ and \mathcal{G}_1 , we apply a DSMA to describe the spin dynamics in a frame rotating with the modulated interaction using a mean-field Hamiltonian (see Appendix A)

$$H_{\text{mf},j} = \rho_0 (1 - \rho_0) \left(\mathcal{G}_0 + \frac{\mathcal{G}_j}{2} \cos \theta_{\text{eff},j} \right) + q_{\text{eff},j} (1 - \rho_0),$$
(1)

where the *j*th-order effective quadratic Zeeman energy is $q_{\rm eff, j} = q - jhf/2$ and the effective spinor phase is $\theta_{\rm eff, j} = \theta + \phi_j$. The use of a DSMA model in this work is motivated by the observation that all three spin components share the same spatial profile as the system evolves in the shallow 1D lattice, with the atoms remaining in the superfluid phase. The established static single-spatial-mode approximation (SSMA) model of spinor BECs in free space [11],

$$H_{\text{mf}}^{\text{FS}} = \rho_0 (1 - \rho_0)(c_2 + c_2 \cos \theta) + q(1 - \rho_0), \qquad (2)$$

is a special case of Eq. (1) in which f=0 and $\mathcal{G}_0=\mathcal{G}_j/2=c_2$. The driven lattice, however, enables independently tuning spin-dependent interactions via \mathcal{G}_0 and \mathcal{G}_j , while the interactions can only be tuned by c_2 in free space (see Appendix A). Crucially, the other key quantities θ and q are also replaced by driven-lattice-defined quantities $\theta_{\mathrm{eff},j}$ and $q_{\mathrm{eff},j}$.

Figures 1(c)–1(e) display typical spin dynamics observed via U-driven sequences near q/h = f/2 = 200 Hz. In the displayed time traces, the period T and amplitude A of spin oscillations vary from relatively small values of T = 3.2(1) ms and A = 0.032(4) at q/h = 160 Hz [Fig. 1(c)] to a diverging period at q/h = 195 Hz [Fig. 1(d)] before returning to small values of T = 8.3(2) ms and A = 0.021(2) as q is further increased to q/h = 235 Hz [Fig. 1(e)]. For the same q region, spin oscillations in free space are drastically different with roughly constant $T \sim 3$ ms and $A \sim 0.015$ [Figs. 1(f)–1(h)].

Figure 2(a) compares spin oscillations observed in free space and via the different driven lattice sequences as a function of q. With U-driven sequences [see triangles in Fig. 2(a)], we observe a single peak centered at a dynamical critical point $q^*/h \approx f/2 = 200$ Hz, characterized by anharmonic oscillations of divergent period separating regions of harmonic spin oscillations for $q < q^*$ and $q > q^*$. In contrast, the observed oscillation period and amplitude in free space [diamonds in

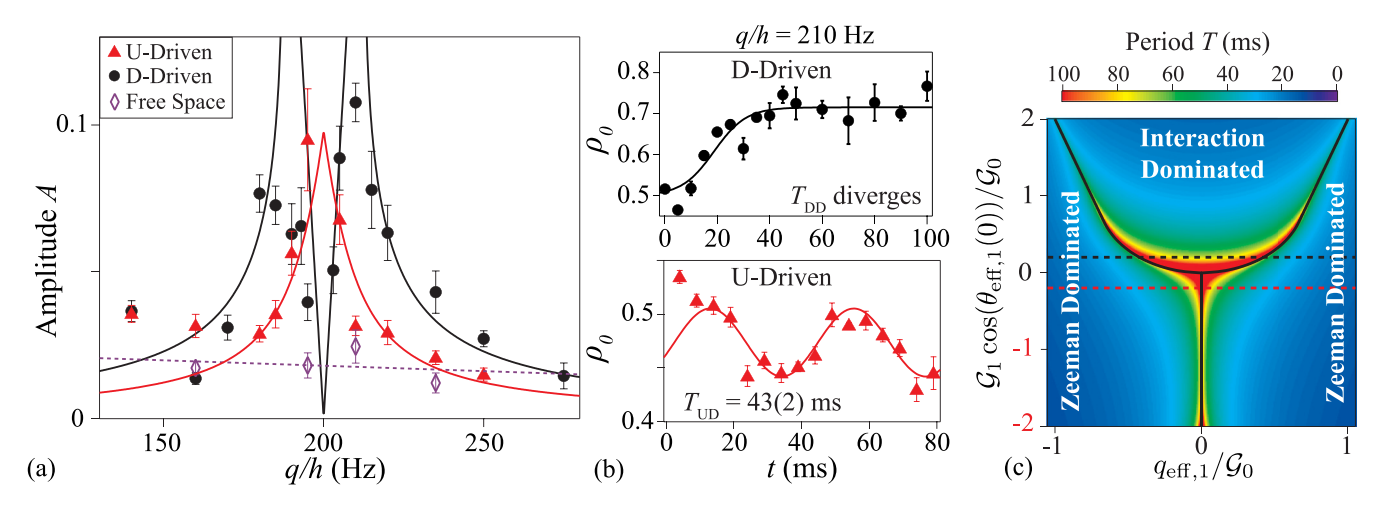


FIG. 2. (a) Triangles, circles, and diamonds display spin oscillation amplitudes observed via U-driven, D-driven, and free-space sequences, respectively, near q/h = f/2 = 200 Hz. Solid lines are DSMA predictions and the dashed line is an eye-guiding linear fit. (b) Drastically different spin dynamics observed via D-driven (upper graph) and U-driven (lower graph) sequences at q/h = 210 Hz. Solid lines are sinusoidal or sigmoidal fits. (c) Phase diagram of $H_{\rm mf,1}$ [see Eq. (1)] for our system demonstrating that the dynamical critical points (black solid lines) for driven lattice systems are determined by $\mathcal{G}_1 \cos[\theta_{\rm eff,1}(0)]/\mathcal{G}_0$. The black and red dashed lines mark $\mathcal{G}_1 \cos[\theta_{\rm eff,1}(0)]/\mathcal{G}_0 = 0.2$ and $\mathcal{G}_1 \cos[\theta_{\rm eff,1}(0)]/\mathcal{G}_0 = -0.2$ for the D-driven and U-driven data, respectively, studied in this paper.

Fig. 2(a)] remain small and slowly decrease with q, consistent with the SSMA predictions [as further elaborated in Fig. 3(a)] [18,23]. Figures 1 and 2(a) therefore demonstrate that U-driven sequences can induce an additional dynamical critical point at a driving-frequency-determined location of $q^*/h \approx f/2$, corresponding to the predicted driven-lattice-induced resonance at $q_{\rm eff,1} = 0$.

Tuning the effective initial phase $\theta_{\mathrm{eff},j}(0)$, although previously much less explored due to technical challenges, can also control spinor dynamics. Our driven lattice system can precisely tune $\theta_{\mathrm{eff},j}(0)$ between 0 and 2π with a step of 4×10^{-4} rad as illustrated by different time traces taken at the same q via U-driven and D-driven sequences [see Fig. 2(b)]. This is further studied in Fig. 2(a): In contrast to U-driven

sequences with only one q^* , two distinct peaks are observed via D-driven sequences [circles in Fig. 2(a)]. These observations agree with the theoretical driven lattice phase diagram derived from Eq. (1) [see Fig. 2(c) and solid lines in Fig. 2(a)], in which the Zeeman-dominated regime, with a characteristic period $T \approx h/2|q_{\rm eff,1}|$, and the interaction-dominated regime, with a T determined by the interactions \mathcal{G}_0 and \mathcal{G}_1 , are split by a critical q^* where T diverges (see Appendix B). When $\theta_{\rm eff,1}(0) = \pi$ and thus $\mathcal{G}_1 \cos[\theta_{\rm eff,1}(0)]/\mathcal{G}_0 = -\mathcal{G}_1/\mathcal{G}_0 < 0$, as realized by U-driven sequences [red dashed line in Fig. 2(c)], the system displays a single q^* at $q_{\rm eff,1} = q - hf/2 = 0$. In contrast, when $\theta_{\rm eff,1}(0) = 0$ and thus $\mathcal{G}_1 \cos[\theta_{\rm eff,1}(0)]/\mathcal{G}_0 = \mathcal{G}_1/\mathcal{G}_0 > 0$, as realized by D-driven sequences [black dashed line in Fig. 2(c)], the system displays two q^* .

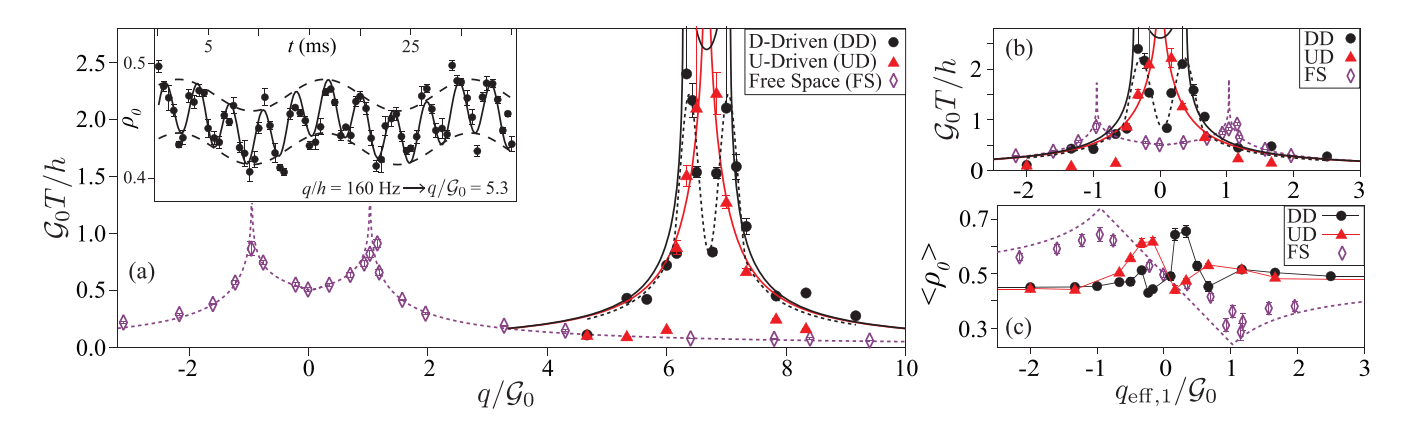


FIG. 3. (a) Triangles, circles, and diamonds display normalized spin oscillation periods observed via U-driven, D-driven, and free-space sequences, respectively. Some free-space data are adapted from our prior work [18]. Black and red solid lines and purple dashed lines are DSMA and SSMA predictions for our initial state, respectively, and the black dashed line is an eye-guiding piecewise fitting. The inset shows the observed dynamics via D-driven sequences at q/h = 160 Hz. The solid line is a two-sine fitting with an overall slow oscillation of $T_{\text{slow}} = 14.5(5)$ ms $\approx h/2|q_{\text{eff},1}|$ determined by $q_{\text{eff},1} = q - hf/2$ plus a fast oscillation of $T_{\text{fast}} = 3.2(1)$ ms $\approx h/2|q_{\text{eff},0}|$ determined by $q_{\text{eff},0} = q$ (see the text for details). The eye-guiding dashed lines display the slow oscillation from the fitting at the extrema. (b) Similar to (a) but plotted against $q_{\text{eff},1}/h = q/h - f/2$. (c) Similar to (b) but for the center of oscillations $\langle \rho_0 \rangle$.

Normalizing q and T by \mathcal{G}_0 enables direct comparisons of the spin dynamics observed in driven and undriven systems, as shown in Fig. 3 with triangles, circles, and diamonds displaying two other characteristics, T and center $\langle \rho_0 \rangle$, of spin oscillations taken with U-driven, D-driven, and free-space sequences, respectively. Here $\langle \rho_0 \rangle$ is extracted from averaging $\rho_0(t)$ over a time trace. Figure 3(a) clearly demonstrates that both driven lattice sequences display significant spin dynamics centered at $q/h \approx f/2 = 200$ Hz $(q/\mathcal{G}_0 \sim 6.7)$ that do not appear in free space.

Another significant difference from free-space dynamics is that, because we only drive $c_2(t)$ approximately sinusoidally (see Appendix C), multiple harmonics have nonzero contributions to the Fourier decomposition, $c_2(t) = \mathcal{G}_0 +$ $\sum_{k=1}^{\infty} \mathcal{G}_k \cos(k2\pi ft - \phi_k)$, and therefore contribute to the spin dynamics. Therefore, time traces taken with a small enough step size often display spin oscillations that are governed by multiple characteristic frequencies associated with different $q_{\text{eff},i}$. For example, the inset in Fig. 3(a) displays an overall slow oscillation, determined by $q_{\text{eff},1} = q - hf/2$, with $T_{\text{slow}} = 14.5(5) \text{ ms} \approx h/2|q_{\text{eff},1}|$ plus a fast oscillation, determined by $q_{\rm eff,0} = q$, with $T_{\rm fast} = 3.2(1)$ ms $\approx h/2|q_{\rm eff,0}|$. Because we are mainly interested in the driven-lattice-induced slow oscillations that are absent in free space, we typically roughly match the step size to the fast oscillation period to highlight the contribution from the closest critical region. This method works well except when q is far from q^* where only a fast oscillation is observed [see Fig. 1(c)], indicating the slow oscillation has an undetectably small amplitude. This may be consistent with DSMA predictions [see Fig. 2(a)].

Plotting the obtained T against $q_{\rm eff,1}$ in Fig. 3(b), interestingly, reveals qualitative similarities between the observed critical regions created by D-driven lattices and in free space, although the critical regions are centered at $q^* \sim \pm \mathcal{G}_0$ in free space and $q_{\rm eff,1}^* \sim \pm 0.37 \mathcal{G}_0 = \pm h \times 11$ Hz for D-driven sequences for the same initial state with $\theta_{\rm eff,1}(0) = 0$. This agrees with the DSMA predicted critical regions that are symmetrically located at $q_{\rm eff,1}^* \sim \pm 0.42 \mathcal{G}_0$ for our D-driven system where $\mathcal{G}_1 \cos[\theta_{\rm eff,1}(0)]/\mathcal{G}_0 \sim 0.2$ [black dashed line in Fig. 2(c)]. Therefore, upon initiating or stopping the D-driven protocol for q between the two symmetric q^* , e.g., 189 Hz < q/h < 211 Hz $(-0.37 < q_{\rm eff,1}/\mathcal{G}_0 < 0.37)$, our system realizes dynamical phase transitions between the Zeemandominated and interaction-dominated regimes [see Figs. 2(a) and 3(b)].

The observed period for U-driven sequences displays a single dynamical critical point at $q_{\rm eff,1}\approx 0$ [see Fig. 3(b)], which also reveals similarities to the predicted free-space spin dynamics for the same initial state with $\theta_{\rm eff,1}(0)=\pi$. Figures 2(a) and 3 therefore demonstrate that the spinor phase can be conveniently tuned by altering the lattice modulation phase ϕ , consistent with Eq. (1) predictions. This ability may also be demonstrated by comparing the behavior of $\langle \rho_0 \rangle$ for each sequence in Fig. 3(c), e.g., $\langle \rho_0 \rangle$ suddenly jumps across the separatrix in U-driven sequences while gradually transitioning between its maximum and minimum values for free space with $\theta_{\rm eff,1}(0)=0$.

While the DSMA provides qualitative insight into the emergence of new dynamical critical points, it does not quantitatively capture several aspects of our observations. For data

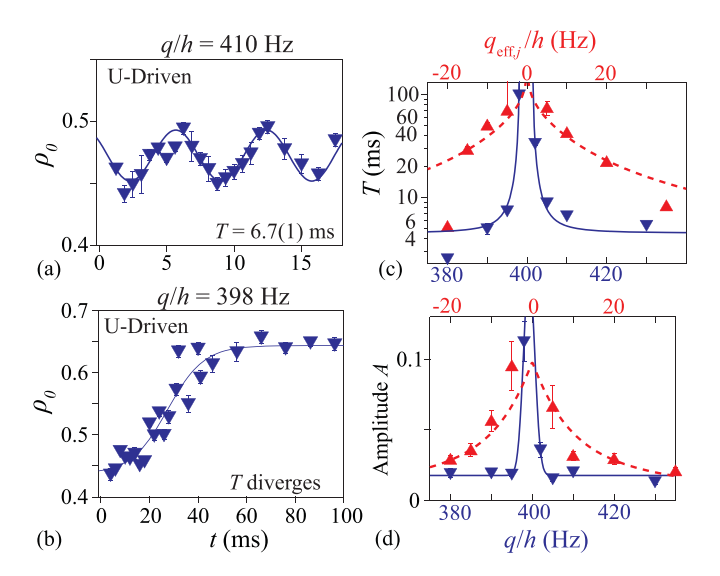


FIG. 4. Time traces taken when q/h equals (a) 410 Hz and (b) 398 Hz, demonstrating a critical region at a higher harmonic with U-driven sequences. Solid lines are sinusoidal or sigmoidal fits. Blue (red) triangles display the (c) oscillation period and (d) amplitude observed via U-driven sequences near $q^*/h \approx 400$ Hz (200 Hz), corresponding to $q_{\rm eff,2} = 0$ ($q_{\rm eff,1} = 0$). The top (bottom) axis is applied to both data sets (blue triangles). Red dashed and blue solid lines are DSMA predictions and eye-guiding Lorentzian fits, respectively (see Appendix D).

taken via D-driven sequences, the observed periods in the interaction-dominated regime are only qualitatively captured by the DSMA. Additionally, the observed $\langle \rho_0 \rangle$ of both driven lattice sequences displays behavior reflected about $q_{\rm eff,1}=0$ from the predictions (see Appendix B). A complete understanding of the observed rich physics requires study with more sophisticated models beyond the DSMA.

Progressively narrower critical regions, due to the much smaller contributions to $c_2(t)$ from higher harmonics, occur in the driven lattice system whenever q/h is an integer multiple of f/2, as demonstrated by two time traces taken near $q^*/h \approx f = 400$ Hz with *U*-driven sequences in Fig. 4. The time traces taken at q/h = 410 Hz [Fig. 4(a)] can be compared to those taken at q/h = 210 Hz [Fig. 2(b)] to reveal that for the same $q_{{\rm eff},j}$, the data taken near $q^*/h \approx f$ $(q_{\rm eff,2}=0)$ have smaller periods and amplitudes than data taken near $q^*/h \approx f/2$ ($q_{\rm eff,1} = 0$). However, the time trace taken at q/h = 398 Hz [see Fig. 4(b)] demonstrates an unmistakable response near a dynamical critical point. We use the oscillation period and amplitude to map the critical region induced by *U*-driven sequences near $q^*/h \approx f = 400 \text{ Hz}$ in Figs. 4(c) and 4(d), respectively, revealing similar, although narrower, signatures to the *U*-driven data taken near $q^*/h \approx$ f/2 = 200 Hz. For example, the width at half maximum of the observed separatrix is around 5 and 20 Hz near $q^*/h \approx$ 400 and 200 Hz in Figs. 4(c) and 4(d), respectively. Critical regions at the higher harmonics, for example, at $q^*/h \approx f$, can therefore be more sensitive to magnetic fields and may have precision sensing applications when combined with the observation that q^* for *U*-driven sequences is determined solely by f.

III. CONCLUSION

We have introduced a versatile technique to simultaneously tune multiple key parameters (namely, spin-dependent interactions $\theta_{\mathrm{eff},j}$ and $q_{\mathrm{eff},j}$) by sinusoidally driving the lattice depth, enabling experimental realizations of dynamical phase transitions with individually tunable spin-preserving and spin-changing collisions. This opens an avenue to the study of engineered Hamiltonians [32–36]. This technique allows the observation of spin dynamics in previously inaccessible parameter regimes, such as high magnetic-field strengths and tunable θ , while overcoming some challenges, for example, detrimental atom losses, associated with other widely used techniques. Cold-atom applications, e.g., in quantum sensing and the study of nonequilibrium dynamics, can be extended over a wide working range by this technique.

ACKNOWLEDGMENTS

D.B. acknowledges support from the National Science Foundation (NSF) through Grant No. PHY-2110158. R.J.L-S. acknowledges support from NSF through Grant No. PHY-2110052 and the Dodge Family College of Arts and Sciences at the University of Oklahoma. J.O.A-H., Z.N.H-S., C.B., and Y.L. acknowledge support from the Noble Foundation and NSF through Grant No. PHY-2207777.

APPENDIX A: DSMA MODEL OF SPINOR BECS IN DRIVEN LATTICES

The dynamics of the spin degree of freedom can be described using a dynamical single-spatial-mode approximation, which accounts for the effects of the time-dependent spatial density profile of the BEC by the time-dependent interaction $c_2(t)$. A full discussion of the DSMA formalism can be found in Ref. [20], with the key result that for a spin-1 BEC it yields an effective Hamiltonian for the spin degree of freedom,

$$\hat{H}_{\text{DSMA}}(t) = \frac{c_2(t)}{N} (\hat{a}_0^{\dagger} \hat{a}_0^{\dagger} \hat{a}_1 \hat{a}_{-1} + \text{H.c.})$$

$$+ \left(\frac{c_2(t)}{N} \hat{a}_0^{\dagger} \hat{a}_0 + q \right) (\hat{a}_1^{\dagger} \hat{a}_1 + \hat{a}_{-1}^{\dagger} \hat{a}_{-1})$$

$$+ \frac{c_2(t)}{2N} (\hat{a}_1^{\dagger} \hat{a}_1 - \hat{a}_{-1}^{\dagger} \hat{a}_{-1})^2.$$
 (A1)

Here \hat{a}_{m_F} ($\hat{a}_{m_F}^{\dagger}$) is the annihilation (creation) operator of an atom in the Zeeman component $m_F = 0, \pm 1$ and N is the total number of atoms in the condensate. The spin-dependent interaction $c_2(t)$ is given by

$$c_2(t) = (N-1)g_2 \int d^3 \mathbf{r} |\psi(\mathbf{r}, t)|^4, \qquad (A2)$$

where $\psi(\mathbf{r},t)$ is the mean-field Gross-Pitaevskii (GP) spatial wave function that is assumed to be identical for all Zeeman components and satisfies the normalization $\int d^3\mathbf{r}|\psi(\mathbf{r},t)|^2 = 1$. The spin-dependent interaction scales with a coupling constant g_2 that is set by the *s*-wave scattering lengths of each spin channel and the mass of sodium [10,25].

In the main text, we considered a driven lattice protocol wherein the lattice amplitude is modulated sinusoidally, $u_L(t) = (u_L^{\max}/2)[1 + \cos(\omega t - \phi)]$, with angular frequency $\omega = 2\pi f$. Assuming that the driving period is slow such that $\hbar\omega$ is small compared to the energy scales of the spin-independent (spatial) dynamics of the BEC, we expect the BEC density profile $|\psi(\mathbf{r},t)|^2$ to change adiabatically with the lattice and thus be modulated periodically. Noting the dependence of Eq. (A2) on the BEC density, we are then motivated to adopt the ansatz for the spin-dependent interaction

$$c_2(t) = \mathcal{G}_0 + \sum_{k=1}^{\infty} \mathcal{G}_k \cos(k\omega t - \phi_k), \tag{A3}$$

where $\mathcal{G}_k > 0$ are the amplitudes of each frequency contribution to the modulation interaction and ϕ_k depends on the initial phase of the lattice ϕ , i.e., whether the lattice is initiated at a minimum (*U*-driven) or maximum (*D*-driven) amplitude, as well as the detailed relationship between the lattice depth and the effective spin-dependent interaction. For our system, $\phi_1 = \phi$ and $\phi_2 = 2\phi + \pi$ (see Appendix C). We assume that $\mathcal{G}_{k\neq 0} < \mathcal{G}_0$ in the following.

Substituting the ansatz (A3) into the DSMA Hamiltonian (A1), we obtain a set of simplified time-independent effective Hamiltonians $\hat{H}_{\text{eff},j}$, which are valid when the Zeeman energy is close to half-integer multiples of the driving energy $\hbar\omega$. We begin by transforming $\hat{H}_{\text{DSMA}}(t)$ into the interaction picture with respect to the Zeeman energy q, yielding

$$\hat{H}_{I}(t) = \frac{\mathcal{G}_{0}}{N} \left[e^{-2iqt/\hbar} \hat{a}_{0}^{\dagger} \hat{a}_{0}^{\dagger} \hat{a}_{1} \hat{a}_{-1} + (\hat{a}_{1}^{\dagger} \hat{a}_{1} - \hat{a}_{-1}^{\dagger} \hat{a}_{-1})^{2} + e^{2iqt/\hbar} \hat{a}_{1}^{\dagger} \hat{a}_{-1}^{\dagger} \hat{a}_{0} \hat{a}_{0} + \hat{a}_{0}^{\dagger} \hat{a}_{0} (\hat{a}_{1}^{\dagger} \hat{a}_{1} + \hat{a}_{-1}^{\dagger} \hat{a}_{-1}) \right]$$

$$+ \sum_{k=1}^{\infty} \frac{\mathcal{G}_{k}}{2N} \left[(e^{-i(k\omega + 2q/\hbar)t + i\phi_{k}} + e^{i(k\omega - 2q/\hbar)t - i\phi_{k}}) \hat{a}_{0}^{\dagger} \hat{a}_{0}^{\dagger} \hat{a}_{1} \hat{a}_{-1} + (e^{i(k\omega + 2q/\hbar)t - i\phi_{k}} + e^{-i(k\omega - 2q/\hbar)t + i\phi_{k}}) \hat{a}_{1}^{\dagger} \hat{a}_{-1}^{\dagger} \hat{a}_{0} \hat{a}_{0} \right]$$

$$+ (e^{-i(k\omega t - \phi_{k})} + e^{i(k\omega t - \phi_{k})}) \hat{a}_{0}^{\dagger} \hat{a}_{0} (\hat{a}_{1}^{\dagger} \hat{a}_{1} + \hat{a}_{-1}^{\dagger} \hat{a}_{-1}) + \frac{1}{2} (e^{-i(k\omega t - \phi_{k})} + e^{i(k\omega t - \phi_{k})}) (\hat{a}_{1}^{\dagger} \hat{a}_{1} - \hat{a}_{-1}^{\dagger} \hat{a}_{-1})^{2} . \tag{A4}$$

Next we assume that the Zeeman energy is tuned close to one of the frequency components of the modulated interaction, i.e., $q \simeq j\hbar\omega/2$, where j is a positive integer such that $q, j\hbar\omega \gg \mathcal{G}_k$. This motivates us to make

a rotating-wave approximation in $\hat{H}_I(t)$ wherein we omit all oscillatory terms except the near-resonant contributions rotating as $2q/\hbar - j\omega$. Finally, we make a unitary transformation with $\hat{U}_i = e^{i(q/\hbar - j\omega/2)t(\hat{a}_1^{\dagger}\hat{a}_1 + \hat{a}_{-1}^{\dagger}\hat{a}_{-1})}$ to obtain the effective

Hamiltonian

$$\begin{split} \hat{H}_{\text{eff},j} &= \hat{U}_{j}^{\dagger} \hat{H}_{I} \hat{U}_{j} - i\hbar \hat{U}_{j}^{\dagger} \frac{\partial \hat{U}_{j}}{\partial t} \\ &= \frac{\mathcal{G}_{0}}{N} \bigg[\hat{a}_{0}^{\dagger} \hat{a}_{0} (\hat{a}_{1}^{\dagger} \hat{a}_{1} + \hat{a}_{-1}^{\dagger} \hat{a}_{-1}) + \frac{1}{2} (\hat{a}_{1}^{\dagger} \hat{a}_{1} - \hat{a}_{-1}^{\dagger} \hat{a}_{-1})^{2} \bigg] \\ &+ \frac{\mathcal{G}_{j}}{2N} (e^{-i\phi_{j}} \hat{a}_{0}^{\dagger} \hat{a}_{0}^{\dagger} \hat{a}_{1} \hat{a}_{-1} + e^{i\phi_{j}} \hat{a}_{0}^{\dagger} \hat{a}_{0}^{\dagger} \hat{a}_{1} \hat{a}_{-1}) \\ &+ q_{\text{eff},j} (\hat{a}_{1}^{\dagger} \hat{a}_{1} + \hat{a}_{-1}^{\dagger} \hat{a}_{-1}), \end{split} \tag{A5}$$

where $q_{{\rm eff},j}=q-j\hbar\omega/2$ is the effective Zeeman energy.

The form of Eq. (A5) should be contrasted with that obtained for a standard spin-1 BEC in the absence of modulated potentials [11], i.e., Eq. (A1) with a constant spin-dependent interaction $c_2(t) \rightarrow c_2$. Three key features are apparent. First, the quadratic Zeeman energy is shifted by the driving frequency of the lattice, as captured by the definition of $q_{\text{eff},j}$. Second, the relative strengths of the spin-preserving and spin-changing interaction terms are now independently controlled by the amplitudes \mathcal{G}_0 and \mathcal{G}_j , respectively. This leads to a distinct dynamical phase diagram, as shown in Fig. 2(c), as the interaction strengths are tuned relative to $q_{\text{eff},j}$. Third, the phase ϕ_j can be used to effectively tune the initial spinor phase that governs the dynamics, as shown in Appendix B.

APPENDIX B: MEAN-FIELD DYNAMICS OF THE DSMA MODEL

Assuming that quantum fluctuations are negligible, which is expected to be true for the initial conditions and observables discussed in the main text, the dynamics generated by the effective Hamiltonian (A5) is conveniently analyzed in the mean-field (classical) limit. Operationally, we obtain the mean-field Hamiltonian by replacing operators by c-numbers in Eq. (A5), $\hat{a}_m \to \alpha_m$ ($\hat{a}_m^\dagger \to \alpha_m^*$), and then defining the canonically conjugate variables $\rho_0 = |\alpha_0|^2/N$ and $\theta = \arg(\alpha_0^{*2}\alpha_1\alpha_{-1})$, yielding

$$H_{\text{mf},j} = \rho_0 (1 - \rho_0) \left(\mathcal{G}_0 + \frac{\mathcal{G}_j}{2} \cos \theta_{\text{eff},j} \right) + q_{\text{eff},j} (1 - \rho_0).$$
(B1)

Here we have defined $\theta_{\mathrm{eff},j} = \theta + \phi_j$ to absorb the phase of the modulated interaction. Note that our mean-field result (B1) is restricted to $M = \rho_1 - \rho_{-1} = (|\alpha_1|^2 - |\alpha_{-1}|^2)/N = 0$, which is a conserved quantity and is zero for all initial states studied in this work.

An analytic solution of the dynamics of $\rho_0(t)$ and $\theta_{\mathrm{eff},j}(t)$ is obtained following methods similar to those used for the standard spin-1 Hamiltonian [11]. We use conservation of energy to eliminate $\theta_{\mathrm{eff},j}(t)$ from the problem and obtain a single differential equation of the form $(\dot{\rho}_0)^2 + V(\rho_0) = 0$ that dictates the dynamics of $\rho_0(t)$. The resulting solutions for the conjugate variables are not insightful for the purposes of this work [37,38] but can be split into two dynamical regimes (phases): (i) a Zeeman-dominated one where the spin oscillation period is set by the effective Zeeman energy $q_{\mathrm{eff},j}$ and (ii) an interaction-dominated one where the spin oscillation period is instead predominantly set by the interaction strengths \mathcal{G}_0 and \mathcal{G}_j . In the classical phase space spanned by $(\rho_0, \theta_{\mathrm{eff},j})$,

these dynamical phases are delineated by a separatrix that is characterized by a divergent spin oscillation timescale. In the following we give expressions for the period and amplitude of spin oscillations and identify the conditions for each dynamical phase to exist as well as the phase boundaries. We split our results into two cases, defined by the lattice phase ϕ_j and assuming an initial condition $(\rho_0(0), \theta_{\text{eff},j}(0)) = (1/2, \phi_j)$.

For $\phi_j = \pi$ (*D*-driven lattice when j = 1) the spin oscillation period is given by

$$T = \frac{2K(k)}{\omega_s},\tag{B2}$$

where K(k) is the complete elliptic integral of the first kind and

$$\omega_{s} = \frac{1}{2} \sqrt{\left(4\mathcal{G}_{0}^{2} - \mathcal{G}_{j}^{2}\right)(a-c)(b-d)}, \quad k = \sqrt{\frac{(a-b)(c-d)}{(a-c)(b-d)}}.$$
(B3)

Here a > b > c > d correspond to the ordered roots $\rho_0^{(n)}$ of the potential $V(\rho_0)$, which are given by

$$\rho_0^{(1)} = \frac{1}{2},$$

$$\rho_0^{(2)} = \frac{1}{2} - \frac{2q_{\text{eff},j}}{2\mathcal{G}_0 - \mathcal{G}_j},$$

$$\rho_0^{(3)} = \frac{1}{2} - \frac{q_{\text{eff},j}}{2\mathcal{G}_0 + \mathcal{G}_j} - \frac{\sqrt{2q_{\text{eff},j}^2 + \mathcal{G}_j^2 + 2\mathcal{G}_0\mathcal{G}_j}}{\sqrt{2}(2\mathcal{G}_0 + \mathcal{G}_j)},$$

$$\rho_0^{(4)} = \frac{1}{2} - \frac{q_{\text{eff},j}}{2\mathcal{G}_0 + \mathcal{G}_j} + \frac{\sqrt{2q_{\text{eff},j}^2 + \mathcal{G}_j^2 + 2\mathcal{G}_0\mathcal{G}_j}}{\sqrt{2}(2\mathcal{G}_0 + \mathcal{G}_j)}.$$
(B4)

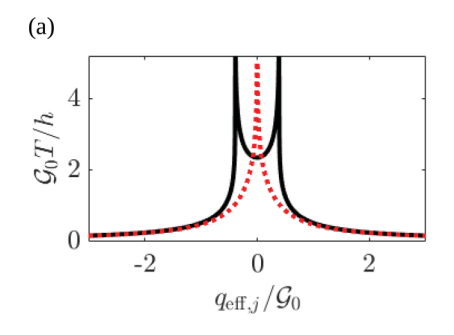
The period T diverges when the effective Zeeman energy is tuned to the value $q_{\mathrm{eff},j}^*=0$ (or equivalently the bare Zeeman energy $q^*=q_{\mathrm{eff},j}^*+j\hbar\omega/2=j\hbar\omega/2$). While this divergence is associated with the initial condition $(\rho_0(0),\theta_{\mathrm{eff},j}(0))=(1/2,\phi_j)$ lying on a separatrix in the classical phase space, it does not demarcate a transition between different dynamical phases. For $\phi_j=\pi$ the dynamics always corresponds to the Zeeman-dominated regime [11]. The oscillation amplitude is given by

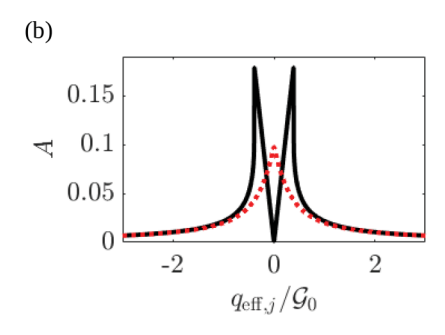
$$\mathcal{A} = \begin{cases} \frac{q_{\text{eff},j}}{2(2\mathcal{G}_0 + \mathcal{G}_j)} + \frac{\sqrt{2q_{\text{eff},j}^2 + \mathcal{G}_j^2 + 2\mathcal{G}_0 \mathcal{G}_j}}{2\sqrt{2}(2\mathcal{G}_0 + \mathcal{G}_j)} & \text{if } q_{\text{eff},j} < 0\\ \frac{q_{\text{eff},j}}{2(2\mathcal{G}_0 + \mathcal{G}_j)} - \frac{\sqrt{2q_{\text{eff},j}^2 + \mathcal{G}_j^2 + 2\mathcal{G}_0 \mathcal{G}_j}}{2\sqrt{2}(2\mathcal{G}_0 + \mathcal{G}_j)} & \text{if } q_{\text{eff},j} > 0, \end{cases}$$
(B5)

which shows a similar peak when the effective Zeeman energy is tuned to $q_{{\rm eff},j}^*$. For $\phi_j=0$ (*U*-driven lattice when j=1) the analytic re-

For $\phi_j = 0$ (*U*-driven lattice when j = 1) the analytic results are limited to the regime $\mathcal{G}_j/\mathcal{G}_0 < 2/3$, which is expected to be applicable for the experimental observations. The spin oscillation period is given by

$$T = \begin{cases} \frac{4K(k)}{\omega_s} & \text{if } |q_{\text{eff},j}| < |q_{\text{eff},j}^*| \\ \frac{2K(k)}{\omega_s} & \text{if } |q_{\text{eff},j}| \geqslant |q_{\text{eff},j}^*|. \end{cases}$$
(B6)





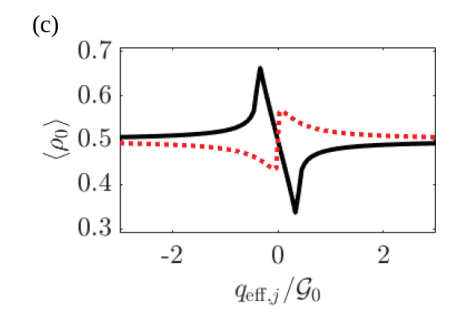


FIG. 5. Analytic predictions for the (a) period, (b) amplitude, and (c) center of spin-mixing oscillations. We use parameters and initial conditions matching the results of Figs. 2 and 3: $\mathcal{G}_0/h = 30\,\text{Hz}$, $\mathcal{G}_1/h = 5\,\text{Hz}$, and $(\rho_0(0), \theta_{\text{eff},1}(0)) = (1/2, \phi_1)$ with phases $\phi_1 = 0$ (black solid lines) and π (red dotted lines).

For $|q_{{\rm eff},j}| < |q_{{\rm eff},j}^*|$ the roots $d = c^*$ are complex and

$$\omega = \sqrt{\left(4\mathcal{G}_0^2 - \mathcal{G}_j^2\right)|(a-c)(b-c)|},$$

$$k = \frac{(a-b)^2 - (|a-c| - |b-c|)^2}{4|(a-c)(b-c)|},$$
(B7)

while for $|q_{{\rm eff},j}|\geqslant |q_{{\rm eff},j}^*|$ all four roots are real and

$$\omega_s = \frac{1}{2} \sqrt{\left(4\mathcal{G}_0^2 - \mathcal{G}_j^2\right)(a-c)(b-d)}, \quad k = \sqrt{\frac{(a-b)(c-d)}{(a-c)(b-d)}}.$$
(B8)

The critical Zeeman energy $q_{\mathrm{eff},j}^* = \pm \sqrt{(2\mathcal{G}_0 - \mathcal{G}_j)\mathcal{G}_j/2}$ marks a dynamical phase transition between the Zeeman-dominated $(|q_{\mathrm{eff},j}| > |q_{\mathrm{eff},j}^*|)$ and interaction-dominated $(|q_{\mathrm{eff},j}| < |q_{\mathrm{eff},j}^*|)$ regimes, at which the period T diverges [11]. The oscillation amplitude is given by

$$\mathcal{A} = \begin{cases} \frac{q_{\text{eff},j}}{2(2\mathcal{G}_0 - \mathcal{G}_j)} + \frac{\sqrt{2q_{\text{eff},j}^2 + \mathcal{G}_j^2 - 2\mathcal{G}_0 \mathcal{G}_j}}{2\sqrt{2}(2\mathcal{G}_0 - \mathcal{G}_j)} & \text{if } q_{\text{eff},j} < -|q_{\text{eff},j}^*| \\ \frac{q_{\text{eff},j}}{2(2\mathcal{G}_0 - \mathcal{G}_j)} - \frac{\sqrt{2q_{\text{eff},j}^2 + \mathcal{G}_j^2 - 2\mathcal{G}_0 \mathcal{G}_j}}{2\sqrt{2}(2\mathcal{G}_0 - \mathcal{G}_j)} & \text{if } q_{\text{eff},j} > |q_{\text{eff},j}^*| \\ \frac{q_{\text{eff},j}}{2\mathcal{G}_0 + \mathcal{G}_j} & \text{if } |q_{\text{eff},j}| < |q_{\text{eff},j}^*| \end{cases}$$
(B9)

and also features a distinguishable peak at $q_{\text{eff},j}^*$.

For reference and a comparison to the data presented in Figs. 2 and 3, we plot examples of the expressions (B2), (B5), (B6), and (B9) in Fig. 5. We use parameters and initial conditions matching those of the experiment of the main text: $G_0/h = 30 \, \text{Hz}$, $G_1/h = 5 \, \text{Hz}$ (obtained from an average of the estimated G_2 in free space and at G_2 in the estimated G_3 in the phase set to G_4 in G_4 (0), G_4 in G_4 (1) with the phase set to G_4 in G_4 (1) with the phase set to G_4 in G_4 (1) with the phase set to G_4 in G_4 (1) with the phase set to G_4 in G_4 (1) with the phase set to G_4 in G_4 (1) with the phase set to G_4 in G_4 (1) with the phase set to G_4 in G_4 (1) with the phase set to G_4 in G_4 (1) G_4 (1) with the phase set to G_4 (1) G_4 (1

While these analytic expressions capture the observations near the first harmonic fairly well, the DSMA model cannot explain the experimental observations near the second resonance at q/h = 400 Hz. A number of factors may contribute to this. For example, our DSMA model assumes well-defined contributions to $c_2(t)$ at integer multiples of the lattice driving frequency, but damping of the modulated interaction,

particularly expected at long hold times in the lattice, should lead to a broader distribution of frequency components. These corrections should contribute more strongly for data taken near q/h = 400 Hz as the second harmonic is expected to have a weak contribution to $c_2(t)$.

APPENDIX C: RELATION BETWEEN LATTICE DEPTH AND INTERACTION STRENGTH

The spin-dependent interaction is implicitly a function of the lattice depth as the latter specifies the spatial density profile of the BEC that arises in Eq. (A2). Thus, one may in principle express the spin-dependent interaction as a power series about the mean lattice depth $u_L^{\rm max}/2$,

$$c_2[u_L(t)] = c_2\left(\frac{u_L^{\text{max}}}{2}\right) + \sum_{n=1}^{\infty} \frac{\beta_n}{n!} \left(\frac{u_L^{\text{max}}}{2}\right)^n \cos^n(\omega t - \phi),$$
(C1)

where

$$\beta_n = \left(\frac{d}{du_L}\right)^n c_2 \bigg|_{u_L = u_T^{\text{max}}/2}.$$
 (C2)

Based on a calculation of $c_2(u_L)$ obtained from 3D GP simulations (see Ref. [20]) of the ground state of a lattice-confined scalar BEC equivalent to that used in the experiment (see Ref. [20]), we expect that the modulation of the interaction approximately follows the sinusoidal behavior of the lattice. This implies that we may truncate our expansion (C1) at order n = 2.

We use the GP simulations to then make two qualitative statements about the expansion coefficients. First, we have that $\beta_1 > 0$, which is consistent with the expectation that the mean-field energy of the condensate [related to the integral $\int d^3 \mathbf{r} |\psi(\mathbf{r})|^4$ that also appears in the definition of c_2 in Eq. (A2)] should increase as the amplitude of the lattice is raised. Second, for our experimental conditions we find $\beta_2 < 0$. These insights are used to rewrite the truncated interaction

$$c_2[u_L(t)] \approx \left[c_2 \left(\frac{u_L^{\text{max}}}{2} \right) + \frac{\beta_2 \left(u_L^{\text{max}} \right)^2}{16} \right]$$

$$+ \frac{\beta_1 u_L^{\text{max}}}{2} \cos(\omega t - \phi)$$

$$+ \frac{\beta_2 \left(u_L^{\text{max}} \right)^2}{16} \cos(2\omega t - 2\phi).$$
 (C3)

This expression is compared with Eq. (A3) to identify

$$\mathcal{G}_0 = c_2 \left(\frac{u_L^{\text{max}}}{2}\right) + \frac{\beta_2 \left(u_L^{\text{max}}\right)^2}{16},$$

$$\mathcal{G}_1 = \frac{\beta_1 u_L^{\text{max}}}{2},$$

$$\mathcal{G}_2 = -\frac{\beta_2 \left(u_L^{\text{max}}\right)^2}{16},$$
(C4)

as well as $\phi_1 = \phi$ and $\phi_2 = 2\phi + \pi$. The latter results are consistent with our prior assumption that $\mathcal{G}_k > 0$ (see Appendix A).

APPENDIX D: DATA ANALYSIS

As mentioned in the main text, we extract the characteristics of the spin dynamics from fitting the observed time evolution of the spin components. The majority of the observed time traces can be well fit by a simple sinusoidal function $\rho_0 = A \sin(2\pi t/T + \beta) + a$. There are three types of exceptions that require modifications to the fitting function. The first exception occurs when q is sufficiently close to a dynamical critical point located at q^* , such as the time traces

shown in the following figures of the main text: Fig. 1(d), the upper panel of Fig. 2(b), and Fig. 4(b). In these cases, we observe that the value of ρ_0 saturates after the initial dynamics. Therefore, we fit these sets with a sigmoidal function $\rho_0 = d + 2A/\{1 + \exp[-(t - T/4)/\tau]\}$. The second exception is that some data sets display a drifting center of oscillation. These sets are fitted by a modified sinusoidal function $\rho_0 = A\sin(2\pi t/T + \beta) + a + bt$ that includes a linear drift of the center of oscillation. The final exception occurs when time traces are taken with a small enough step size. These time traces often display spin oscillations that are governed by multiple characteristic frequencies associated with different $q_{\rm eff, \it j}$ and thus can be fitted by a sum of multiple sinusoidal functions.

Although the DSMA model explains many of our observations at the critical regions near q/h = f/2 = 200 Hz and predicts a sequence of critical regions at higher harmonics due to the lattice modulation, the quantitative predictions of the model disagree with some experimental observations, e.g., the narrow width of the resonance at q/h = f = 400 Hz generated by the second harmonic. A number of factors may contribute to this discrepancy (see the discussion at the end of Appendix B). We therefore use a Lorentzian fit to the data in Fig. 4 to estimate the location and width of the resonance.

- Q. Guan and R. J. Lewis-Swan, Identifying and harnessing dynamical phase transitions for quantum-enhanced sensing, Phys. Rev. Res. 3, 033199 (2021).
- [2] L. Zhou, J. Kong, Z. Lan, and W. Zhang, Dynamical quantum phase transitions in a spinor Bose-Einstein condensate and criticality enhanced quantum sensing, Phys. Rev. Res. 5, 013087 (2023).
- [3] B. Evrard, A. Qu, J. Dalibard, and F. Gerbier, Observation of fragmentation of a spinor Bose-Einstein condensate, Science **373**, 1340 (2021).
- [4] D. R. Romano and E. J. V. de Passos, Population and phase dynamics of F = 1 spinor condensates in an external magnetic field, Phys. Rev. A **70**, 043614 (2004).
- [5] Z. N. Hardesty-Shaw, Q. Guan, J. O. Austin-Harris, D. Blume, R. J. Lewis-Swan, and Y. Liu, Nonlinear multi-state tunneling dynamics in a spinor Bose-Einstein condensate, Phys. Rev. A 108, 053307 (2023).
- [6] L. Zhao, T. Tang, Z. Chen, and Y. Liu, Lattice-induced rapid formation of spin singlets in spin-1 spinor condensates, arXiv:1801.00773.
- [7] J. O. Austin, Z. N. Shaw, Z. Chen, K. W. Mahmud, and Y. Liu, Manipulating atom-number distributions and detecting spatial distributions in lattice-confined spinor gases, Phys. Rev. A 104, L041304 (2021).
- [8] M.-S. Chang, Q. Qin, W. Zhang, L. You, and M. S. Chapman, Coherent spinor dynamics in a spin-1 Bose condensate, Nat. Phys. 1, 111 (2005).
- [9] J. O. Austin, Z. Chen, Z. N. Shaw, K. W. Mahmud, and Y. Liu, Quantum critical dynamics in a spinor Hubbard model quantum simulator, Commun. Phys. 4, 61 (2021).

- [10] Z. Chen, T. Tang, J. Austin, Z. Shaw, L. Zhao, and Y. Liu, Quantum quench and nonequilibrium dynamics in lattice-confined spinor condensates, Phys. Rev. Lett. 123, 113002 (2019).
- [11] W. Zhang, D. L. Zhou, M.-S. Chang, M. S. Chapman, and L. You, Coherent spin mixing dynamics in a spin-1 atomic condensate, Phys. Rev. A 72, 013602 (2005).
- [12] J. Kronjäger, C. Becker, P. Navez, K. Bongs, and K. Sengstock, Magnetically tuned spin dynamics resonance, Phys. Rev. Lett. 97, 110404 (2006).
- [13] A. T. Black, E. Gomez, L. D. Turner, S. Jung, and P. D. Lett, Spinor dynamics in an antiferromagnetic spin-1 condensate, Phys. Rev. Lett. 99, 070403 (2007).
- [14] Y. Liu, S. Jung, S. E. Maxwell, L. D. Turner, E. Tiesinga, and P. D. Lett, Quantum phase transitions and continuous observation of spinor dynamics in an antiferromagnetic condensate, Phys. Rev. Lett. 102, 125301 (2009).
- [15] H. K. Pechkis, J. P. Wrubel, A. Schwettmann, P. F. Griffin, R. Barnett, E. Tiesinga, and P. D. Lett, Spinor dynamics in an antiferromagnetic spin-1 thermal Bose gas, Phys. Rev. Lett. 111, 025301 (2013).
- [16] X. He, B. Zhu, X. Li, F. Wang, Z.-F. Xu, and D. Wang, Coherent spin-mixing dynamics in thermal ⁸⁷Rb spin-1 and spin-2 gases, Phys. Rev. A **91**, 033635 (2015).
- [17] J. Jiang, L. Zhao, S.-T. Wang, Z. Chen, T. Tang, L.-M. Duan, and Y. Liu, First-order superfluid-to-Mott-insulator phase transitions in spinor condensates, Phys. Rev. A 93, 063607 (2016).
- [18] L. Zhao, J. Jiang, T. Tang, M. Webb, and Y. Liu, Dynamics in spinor condensates tuned by a microwave dressing field, Phys. Rev. A 89, 023608 (2014).

- [19] L. Zhao, J. Jiang, T. Tang, M. Webb, and Y. Liu, Antiferromagnetic spinor condensates in a two-dimensional optical lattice, Phys. Rev. Lett. 114, 225302 (2015).
- [20] Z. N. Hardesty-Shaw, Q. Guan, J. O. Austin, D. Blume, R. J. Lewis-Swan, and Y. Liu, Quench-induced nonequilibrium dynamics of spinor gases in a moving lattice, Phys. Rev. A 107, 053311 (2023).
- [21] J. Jiang, L. Zhao, M. Webb, and Y. Liu, Mapping the phase diagram of spinor condensates via adiabatic quantum phase transitions, Phys. Rev. A **90**, 023610 (2014).
- [22] Y. Kawaguchi and M. Ueda, Spinor Bose-Einstein condensates, Phys. Rep. 520, 253 (2012).
- [23] D. M. Stamper-Kurn and M. Ueda, Spinor Bose gases: Symmetries, magnetism, and quantum dynamics, Rev. Mod. Phys. 85, 1191 (2013).
- [24] C. Chin, R. Grimm, P. Julienne, and E. Tiesinga, Feshbach resonances in ultracold gases, Rev. Mod. Phys. 82, 1225 (2010).
- [25] S. Knoop, T. Schuster, R. Scelle, A. Trautmann, J. Appmeier, M. K. Oberthaler, E. Tiesinga, and E. Tiemann, Feshbach spectroscopy and analysis of the interaction potentials of ultracold sodium, Phys. Rev. A 83, 042704 (2011).
- [26] L. Santos, M. Fattori, J. Stuhler, and T. Pfau, Spinor condensates with a laser-induced quadratic Zeeman effect, Phys. Rev. A 75, 053606 (2007).
- [27] S. R. Leslie, J. Guzman, M. Vengalattore, J. D. Sau, M. L. Cohen, and D. M. Stamper-Kurn, Amplification of fluctuations in a spinor Bose-Einstein condensate, Phys. Rev. A 79, 043631 (2009).
- [28] F. Gerbier, A. Widera, S. Fölling, O. Mandel, and I. Bloch, Resonant control of spin dynamics in ultracold quantum gases by microwave dressing, Phys. Rev. A **73**, 041602(R) (2006).

- [29] E. M. Bookjans, A. Vinit, and C. Raman, Quantum phase transition in an antiferromagnetic spinor Bose-Einstein condensate, Phys. Rev. Lett. **107**, 195306 (2011).
- [30] J. Marino, M. Eckstein, M. Foster, and A.-M. Rey, Dynamical phase transitions in the collisionless pre-thermal states of isolated quantum systems: Theory and experiments, Rep. Prog. Phys. 85, 116001 (2022).
- [31] R. J. Lewis-Swan, S. R. Muleady, D. Barberena, J. J. Bollinger, and A. M. Rey, Characterizing the dynamical phase diagram of the Dicke model via classical and quantum probes, Phys. Rev. Res. 3, L022020 (2021).
- [32] K. Fujimoto and S. Uchino, Floquet spinor Bose gases, Phys. Rev. Res. 1, 033132 (2019).
- [33] Y. Zhang, Y. Chen, H. Lyu, and Y. Zhang, Quantum phases in spin-orbit-coupled Floquet spinor Bose gases, Phys. Rev. Res. 5, 023160 (2023).
- [34] B. Evrard, A. Qu, K. Jiménez-García, J. Dalibard, and F. Gerbier, Relaxation and hysteresis near Shapiro resonances in a driven spinor condensate, Phys. Rev. A 100, 023604 (2019).
- [35] Z.-C. Li, Q.-H. Jiang, Z. Lan, W. Zhang, and L. Zhou, Non-linear Floquet dynamics of spinor condensates in an optical cavity: Cavity-amplified parametric resonance, Phys. Rev. A 100, 033617 (2019).
- [36] S. M. Jose, K. Sah, and R. Nath, Patterns, spin-spin correlations and competing instabilities in driven quasi-two-dimensional spin-1 Bose-Einstein condensates, Phys. Rev. A 108, 023308 (2023).
- [37] A. M. Sánchez, J. D. Bejarano, and D. C. Marzal, Solution of the anharmonic quartic potential oscillator problem, J. Sound Vib. **161**, 19 (1993).
- [38] P. F. Byrd and M. D. Friedman, *Handbook of Elliptic Integrals for Engineers and Physicists* (Springer, Berlin, 1954).